

TECHNICAL RESEARCH REPORT

Spatially Resolved Compressor Characteristics for Modeling and Control of Blade-Scale Flow Instabilities

by R.A. Adomaitis

T.R. 95-44



*Sponsored by
the National Science Foundation
Engineering Research Center Program,
the University of Maryland,
Harvard University,
and Industry*

Spatially Resolved Compressor Characteristics for Modeling and Control of Blade-Scale Flow Instabilities

Raymond A. Adomaitis

Institute for Systems Research
University of Maryland
College Park, MD 20742

adomaiti@isr.umd.edu

December 19, 1995

Abstract

A numerical technique capable of simulating blade-scale compression system flow instabilities over times scales spanning tens of rotor revolutions is presented. Simulations of stall inception, growth to fully-developed rotating stall, and evidence for hysteresis, secondary instabilities, and other nonlinear phenomena are presented. Signal processing techniques for flow asymmetry characterization are discussed in the context of obtaining low-order representations of the flow disturbances with the ultimate goal of active stall suppression.

Keywords: compressor stall, instabilities, bifurcations, computational fluid dynamics, coherent structures

1 Introduction

Models for understanding the aerodynamics of compression system stall inception and growth of these disturbances to fully-developed rotating stall have existed for over forty years. A feature common to many of these models is that the power input to the flow field is modeled by some forcing function to the equations of fluid motion [1, 2]. This “indirect” approach is favored over direct numerical simulation because of the wide time scale range of the dynamic phenomena (several revolutions for stall, 10-100’s for a surge cycle) and the complexity of direct computational fluid dynamic simulations of multistage compression systems.

Recently, numerical techniques which represent the force imparted to fluid flow fields as forcing functions to the Navier-Stokes equations [3] (replacing boundary conditions in the flow and pressure fields) have been developed for simulating systems with fluid/flexible structure interactions [4]. Because the speed with which fluid dynamic simulations can be performed increases with decreasing complexity of the domain over which the computations are performed, these techniques can also improve the efficiency of these computations. Exploitation of the interplay of this numerical technique and the communication patterns of massively-parallel processors is a key element in making the multistage compressor simulations possible in this work.

The modeling approach presented in this study is unique in the field of turbocompressor simulation in that not only do the forcing functions depend on spatial position, but they are also computed solely from the equations of fluid motion and the geometry of the compressor blading. An important aspect of this work is studying the *predictive* capabilities of such a model in simulating the inception of rotating stall as the stall margin is crossed, and following the growth of these instabilities to fully-developed rotating stall. Simulations of rotor blade wake momentum defect growth to a fully separated flow field blocking a blade passage will be shown to be consistent with the conceptual model of compressor stall, originally proposed by Iura and Rannie [5]. Stall cell propagation rates of approximately 1/2 rotor speed were observed in our simulations. The stall cell propagation mechanism put forth by the cited study¹ corroborates with our simulations.

The simulation results presented in this paper focus on a two stage compression system model. Each rotor row consists of 11 blades and each stator has 14 blades. The number of blades was chosen to exceed the minimum number of rotor blades involved in a propagating modal stall cell: Longley [6] estimated that the minimum wavelength of a modal stall disturbance would span eight blades, and this theoretical prediction is supported by experimental studies with a seven rotor blade machine [7] which resulted in stall events consistent with the continuum models of Moore and Greitzer [1]. Naturally, smaller-scale events should then be captured in our design.

Understanding the spatial structure of the stall cells is important for interpreting signals obtained from a finite number of measurement probes in experimental systems and is particularly important for designing stall controllers based on direct suppression of these flow disturbances. Early studies of the spatial structure of stall cells assumed single *sin*-shaped modes, and studies which built on this initial work decomposed the stall cells into modes of a truncated Fourier series. We will present preliminary results on obtaining an optimal (empirically determined) set of basis functions from our detailed simulations, a technique which has the potential of generating extremely low order simulators which retain virtually all of the fidelity of the original simulations.

2 The Numerical Simulation Technique

The compression system model developed in this paper is based on 2D, incompressible flow through an annulus, and so we begin by writing the Navier-Stokes equations in conservative form and separating the right-hand-side into terms which are linear and nonlinear in the velocity field \mathbf{v} to obtain

$$\frac{\partial \mathbf{v}}{\partial t} = -\nabla \cdot (\mathbf{v}\mathbf{v}) + \frac{1}{R_e} \nabla^2 \mathbf{v} - \nabla p + \mathbf{f} = \mathbf{N}(\mathbf{v}) + \mathbf{L}(\mathbf{v}) - \nabla p + \mathbf{f} \quad (1)$$

over the unit square. What follows is an outline of the numerical technique used to integrate (1) over one time step Δt . The time step of all simulations performed in this study was fixed at 0.001 rotor revolutions. A staggered arrangement of velocity component discretization points was used in the finite-difference calculation of the spatial derivatives [8]. Pressure and forcing function scalar field values were defined at the cell centers using a 500×500 evenly spaced array of cells. Dimensionless rotor speed is 1.0 and the Reynolds number based on the circumferential length was set at $R_e = 10,000$.

At the start of each time step, given a velocity field \mathbf{v}^n at time t_n and following the operator splitting method of Karniadakis and co-workers [9], we predict an interim velocity field $\hat{\mathbf{v}}$ from

¹The mean flow field diverted around the blockage results in blades to one side experiencing increased angles of attack, thus inducing flow separation, and blades to the other side experiencing the opposite effect, resulting in overall stall cell propagation in the former direction

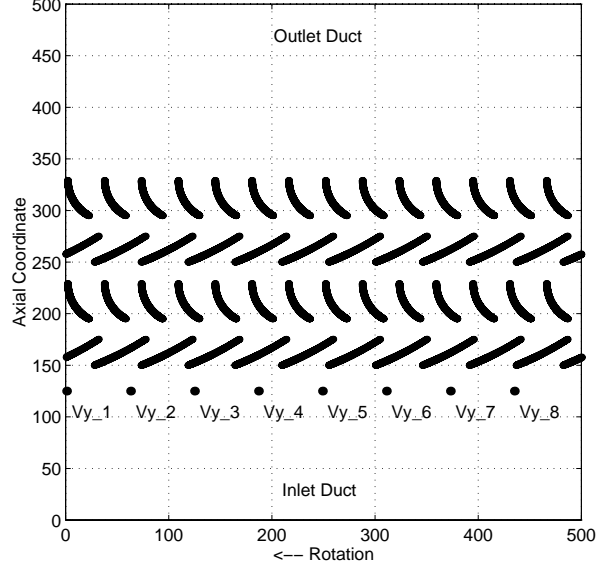


Figure 1: Compression system geometry on the discretization grid points. Mean axial flow is from bottom to top. Rotors: 1st and 3rd blade rows; stators are 2nd and 4th. Vy_n marks the axial velocity measurement locations.

a fourth-order Runge-Kutta (explicit) step:

$$\frac{\hat{\mathbf{v}} - \mathbf{v}^n}{\Delta t} = \frac{1}{6}(\mathbf{k}_0 + 2\mathbf{k}_1 + 2\mathbf{k}_2 + \mathbf{k}_3)$$

with

$$\begin{aligned} \mathbf{k}_0 &= \mathbf{N}(\mathbf{v}^n) & \mathbf{k}_2 &= \mathbf{N}(\mathbf{v}^n + \mathbf{k}_1 \Delta t / 2) \\ \mathbf{k}_1 &= \mathbf{N}(\mathbf{v}^n + \mathbf{k}_0 \Delta t / 2) & \mathbf{k}_3 &= \mathbf{N}(\mathbf{v}^n + \mathbf{k}_2 \Delta t). \end{aligned}$$

Adding the contributions of the pressure and forcing fields gives

$$\frac{\hat{\mathbf{v}} - \hat{\mathbf{v}}}{\Delta t} = -\nabla \hat{p} + \mathbf{f}_b + \mathbf{f}_t \quad \text{with} \quad \mathbf{f}_t \cdot \mathbf{e}_y = \left(\frac{V}{\gamma}\right)^2 \quad (2)$$

where \mathbf{f}_t acts only in the direction \mathbf{e}_y of the mean axial flow and is applied over the entire flow field as a substitute for the atmospheric-to-plenum pressure rise. V is the mean axial outlet velocity component, and γ is the throttle position in the orifice equation.

The spatially resolved forcing function \mathbf{f}_b is computed to impart the equivalent amount of force that would otherwise be “felt” by the fluid if the fluid/blade boundary condition actually existed. If \mathbf{x} is the vector of k discretization points defining an individual rotor or stator blade, $\hat{\mathbf{v}}(\mathbf{x}_i)$ is the interim velocity field *interpolated* to the discretization point \mathbf{x}_i , and \mathbf{v}_i^* is the blade velocity,

$$\sum_{j=1}^k \delta(\mathbf{x}_i, \mathbf{x}_j) \mathbf{f}_b(\mathbf{x}_j) = \frac{\mathbf{v}_i^* - \hat{\mathbf{v}}(\mathbf{x}_i)}{\Delta t}.$$

Solving this system of linear equations for the individual forces \mathbf{f}_{b_i} is numerically efficient, since the array of δ values only must be inverted once. This numerical simplification is possible since the arrangement of forcing points on each blade remains constant, and because the blades are far enough from each other so that their force fields do not overlap. The numerical distance function

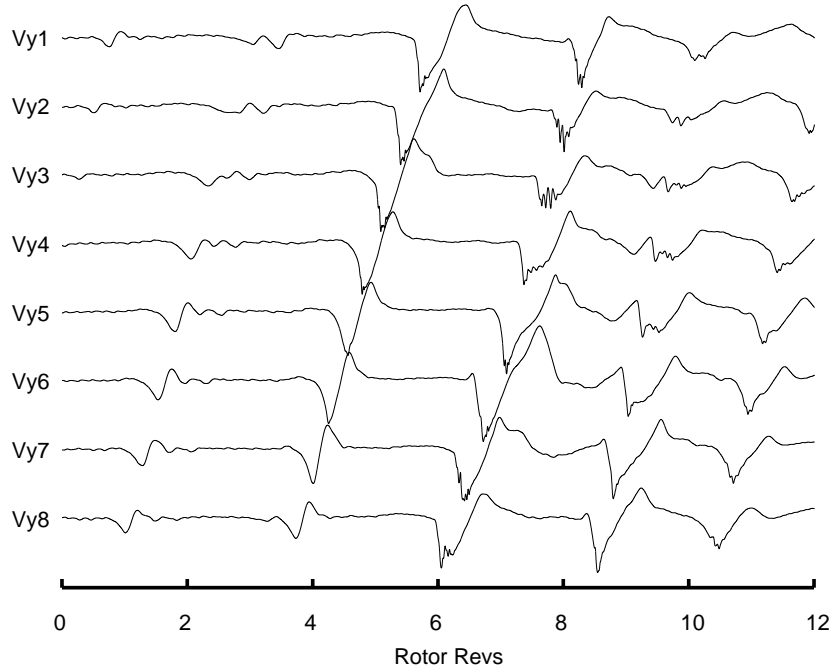


Figure 2: Stall inception after throttle position change from $\gamma = 0.3$ to $\gamma = 0.2$.

$\delta(\mathbf{x}_i, \mathbf{x}_j)$ used above, in calculating $\hat{\mathbf{v}}(\mathbf{x}_i)$, and for spreading $\mathbf{f}_{\mathbf{b}}$ to the pressure discretization point locations is discussed in Peskin [4].

Continuity is enforced by taking the divergence of (2) and solving the resulting Poisson's equation for the static pressure field p :

$$\nabla^2 \hat{p} = \frac{\nabla \cdot \hat{\mathbf{v}}}{\Delta t} + \nabla \cdot \mathbf{f}_{\mathbf{b}}. \quad (3)$$

Solving the (spatially) discretized form of (3) amounts to solving 250,000 coupled, linear, algebraic equations – a large number resulting from the fine mesh size. This means iterative solution methods must be used over a direct method, such as Gaussian elimination. Because we have replaced what would otherwise be a complicated, time-dependent geometry with forcing functions defined over a simple domain, we can take advantage of relatively non-memory intensive and naturally parallelizable techniques, such as the Conjugant Gradient Method. A simple domain means less use of routed and more nearest-neighbor communications in massively-parallel processors, and so we have found significant advantages to performing our simulations, written in CM Fortran, on a Thinking Machines Corporation CM5.

The final step in computing the total update also benefits from fast linear equation solvers since we chose to use an implicit integrator for calculating the contribution of the linear portion of (1):

$$\frac{\mathbf{v}^{n+1} - \hat{\mathbf{v}}}{\Delta t} = \mathbf{L}(\mathbf{v}^{n+1}).$$

This concludes the discussion of the numerical integration technique.

3 Simulation Results

One of the hallmarks of compression system aerodynamic instabilities is the hysteresis associated with compressor stall. In a noise-free situation, we find that as the compressor throttle is closed, the plenum-to-atmospheric pressure rises while the mean axial flow decreases until the axisymmetric flow field becomes unstable. After this point is crossed, small perturbations grow rapidly into large-amplitude rotating stall cells. Reopening the throttle does not necessarily reverse this transition: the *multistability* brought about by the nonlinear nature of the instabilities can lead to nonrecoverable stall and operating points which are unstable with respect to finite amplitude disturbances. Noise clouds the stall inception picture, since small amplitude inlet flow field disturbances can be amplified by the impending instability and may give rise to the frequently cited, long-lived, small amplitude stall precursors.

Preliminary simulations were performed to find the approximate location of the stall inception point. The compression system simulator was then brought to equilibrium at a throttle opening corresponding to $\gamma = 0.3$, a “uniform-flow,” locally asymptotically stable operating point (we place the term uniform-flow in quotes since the velocity field, even in the inlet and exits ducts, is never truly uniform due to flow around the compressor blading). The throttle was then closed through the range where the flow was found to become unstable to a final value of $\gamma = 0.2$. The time trace of Fig. 2 shows the onset of stall soon afterwards. Note that the disturbance grows to a large-amplitude rotating stall cell after only a few rotor revolutions, growing only out of the natural flow asymmetry induced by the rotor-stator blade interactions. The early state of this flow disturbance is illustrated in Fig. 5.

After a period of disturbance growth to fully developed rotating stall, the throttle was reopened to $\gamma = 0.3$ (recall that this throttle position corresponds to a *locally* asymptotically stable uniform flow operating point). After reaching equilibrium, we found that the rotating stall persisted, a clear indicator of multistability (hysteresis). See Fig. 3 for a close-up view of the stalled flow field. Furthermore, plotting the mean exit pressure versus time (Fig. 4) shows a secondary, time-dependent oscillation. Because the frequency is so much lower than the frequency with which stall cells interact with individual rotor blades, we take this as evidence of secondary bifurcations taking place along the stalled-flow equilibria locus born off the axisymmetric flow solution branch. Because of the incompressible formulation of this simulation, the exit duct does not act as a mass storage region and so this is not a surge bifurcation, but results from the birth of a modulated traveling wave. See Adomaitis and Abed[10] for more details on the bifurcation behavior of these systems.

4 Signal Processing

One of the primary motivations for this research was to develop a compression system flow instability simulator with no built-in bias towards the structure of the stall inception and fully developed flow field instabilities. This approach would give a model capable of resolving both modal and localized disturbances, and so would provide an effective tool for developing numerical techniques for characterizing the flow asymmetry and testing signal processing techniques for identifying such flow features in an experimental rig. To this end, consider the problem of finding a set of spatially-dependent trial functions $\psi_i(x)$ from which a time-dependent linear combination can be computed to represent the the axial component of flow field (V_y):

$$V_y(x, t) = a_0(t)\psi_0(x) + a_1(t)\psi_1(x) + \dots + a_m(t)\psi_m(x).$$

Taking $\psi_0 = 1$ means a_0 represents the mean axial flow V_{mean} , and all ψ_i for $i = 1, 2, \dots$ represent spatially-varying modes, so

$$v(x, t) = a_1(t)\psi_1(x) + \dots + a_m(t)\psi_m(x). \tag{4}$$

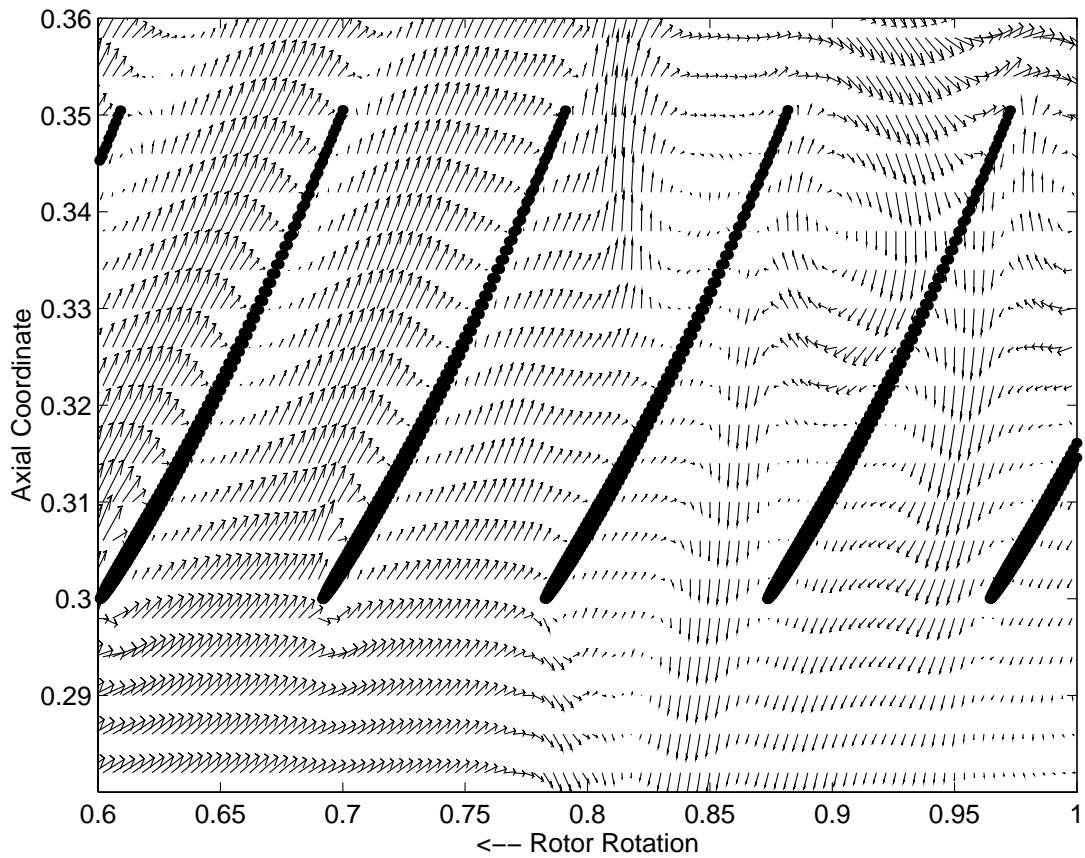


Figure 3: Stable flow field *relative to rotor 1*, illustrating stalled and unstalled blade passages (to the right and left, respectively) for $\gamma = 0.3$. The stall cell propagates to the right in this reference frame. Note the region of reversed flow upstream of the stall cell.

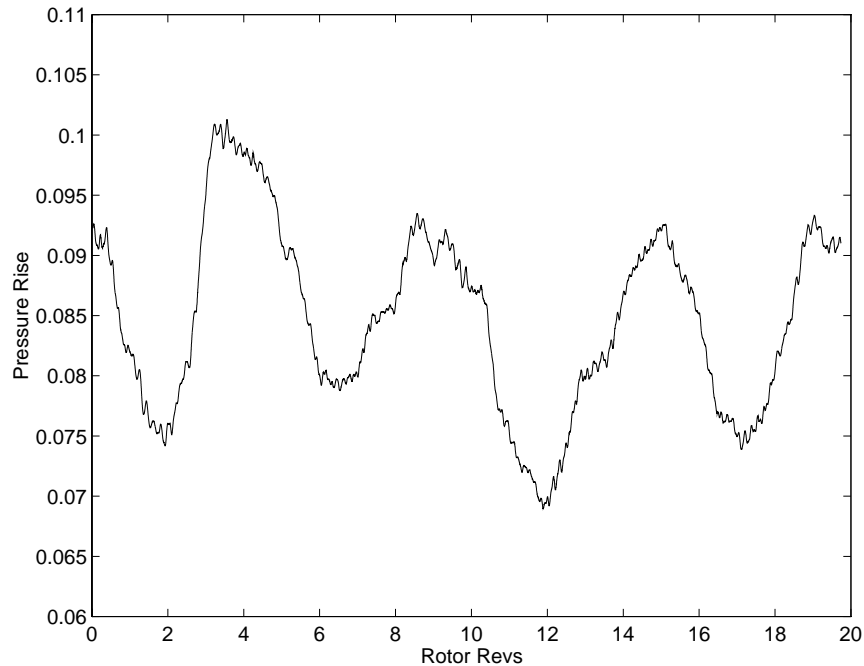


Figure 4: Plenum-to-atmospheric pressure trace during rotating stall for $\gamma = 0.3$. The 6-rev oscillations (a much lower frequency than that generated by stall cells passing from blade-to-blade) indicates secondary instabilities.

Ultimately, we will consider low-order approximations to the entire 2D flow field, but this study will be limited to a 1D “slice” across the circumferential coordinate at the axial position of the velocity measurement probes (see Fig. 5). Taking snapshots of the instantaneous axial velocity component of the flow field deviations at this location facilitates comparisons to previous studies, such as Moore and Greitzer[1] where the flow field disturbance just upstream of the inlet guide vanes was modeled.

Because finite difference approximations were used to discretize (1), each snapshot taken during the stall inception transient of Fig. 3 consists of a long (500 element) vector of velocity values. Each of these vectors corresponds to points in time separated by approximately $1/3$ rotor rev intervals, giving a total of $M = 43$ snapshots collected during the 12 rotor rev transient. Prior to applying the numerical technique to be discussed, we estimate the phase angle of the flow field disturbances and adjust all of snapshots to synchronize the phase angles so that the minimum velocity point all coincide at the V_{y_8} probe position.

The time evolution of the flow field is governed by set a well-behaved differential equations and so there is some degree of correlation between the snapshots. This means the snapshots are not necessarily linearly independent, and so an efficient method for representing the snapshot vectors is to first determine an orthogonal basis spanning the snapshots and then decompose the snapshots using the basis vectors as discretized trial functions. One can use the Gram-Schmidt orthogonalization procedure to obtain the basis vectors, but an optimal basis is determined by a computationally efficient implementation of the Proper Orthogonal Decomposition method discussed in Sirovich [11].

If the vector v_i represents the deviation of the axial flow component V_y from the mean axial

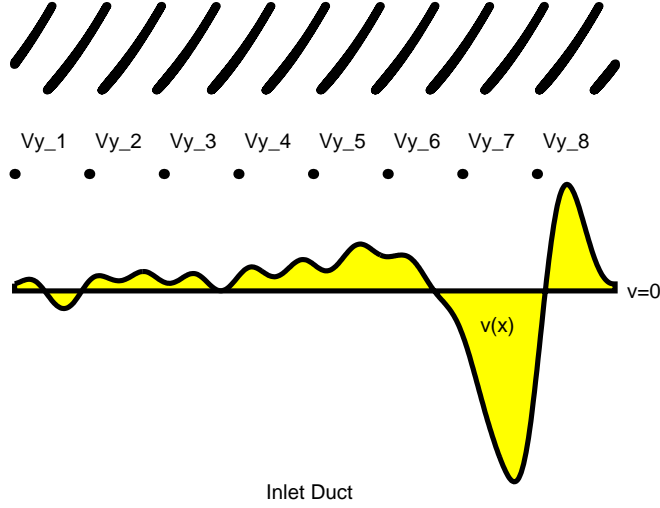


Figure 5: Flow field axial velocity component deviation in the inlet duct at the axial position of the velocity measurement probes Vy_n .

flow V_{mean} of snapshot i , we can construct the array of inner products:

$$\begin{bmatrix} (v_1, v_1) & (v_1, v_2) & \cdots & (v_1, v_M) \\ (v_2, v_1) & (v_2, v_2) & \cdots & (v_2, v_M) \\ \vdots & \vdots & \ddots & \vdots \\ (v_M, v_1) & (v_M, v_2) & \cdots & (v_M, v_M) \end{bmatrix} \quad (5)$$

and so determine the optimal set of eigenmodes spanning the original set of snapshots using the eigenvectors E_i of (5). Each element $E_{j,i}$ gives the contribution of snapshot j to eigenmode i , and so the empirical eigenfunctions are computed by

$$\psi_i(x) = \sum_{j=1}^M E_{j,i} v_j(x).$$

These eigenfunctions are shown in Fig. 6.

With each eigenmode ψ_i is associated an eigenvalue λ_i which corresponds to the probability of finding that eigenfunction in the time-dependent flow field from which the snapshots were extracted:

$$\lambda_i = [(v_1, \psi_i)^2 + (v_2, \psi_i)^2 + \dots + (v_M, \psi_i)^2]/M.$$

An optimal set of trial functions should capture as much energy as possible in as few modes as

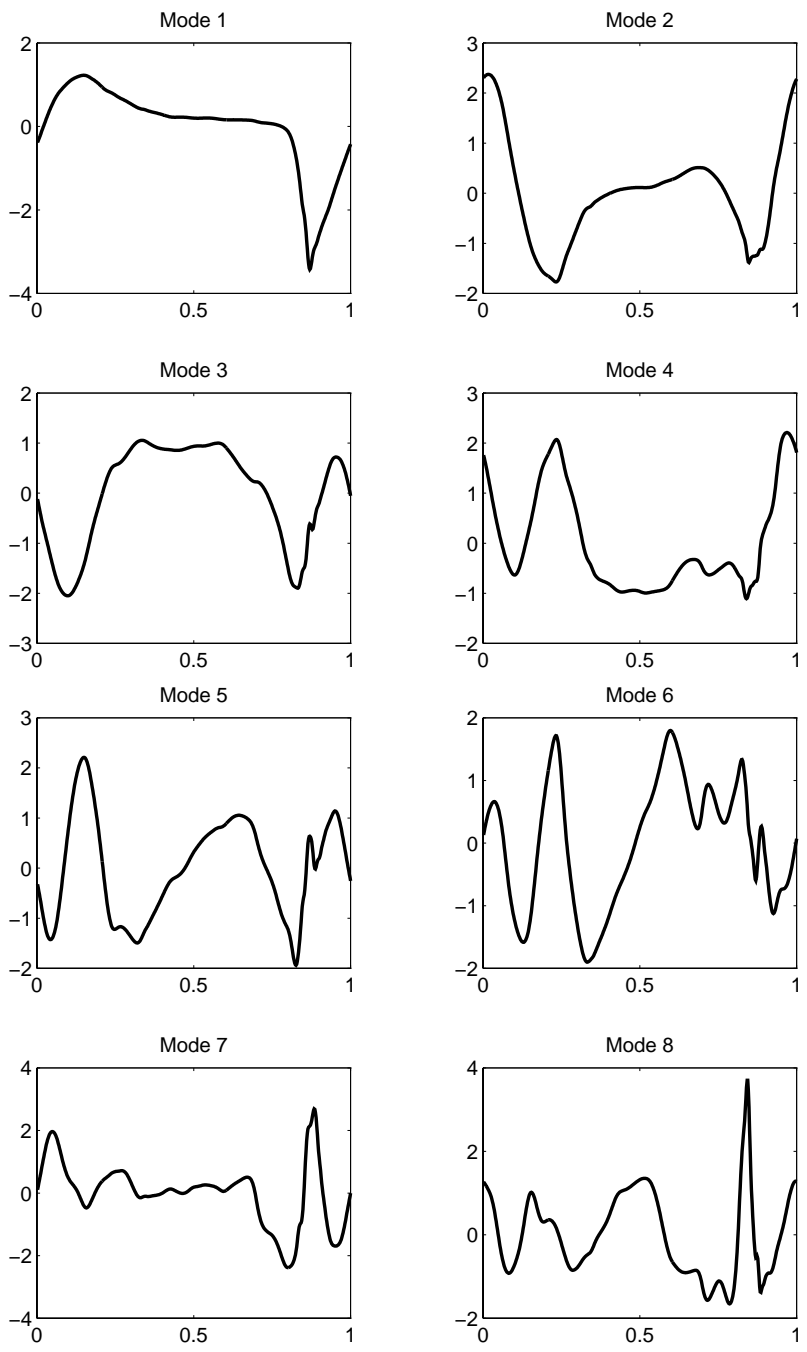


Figure 6: First eight empirically-determined eigenmodes.

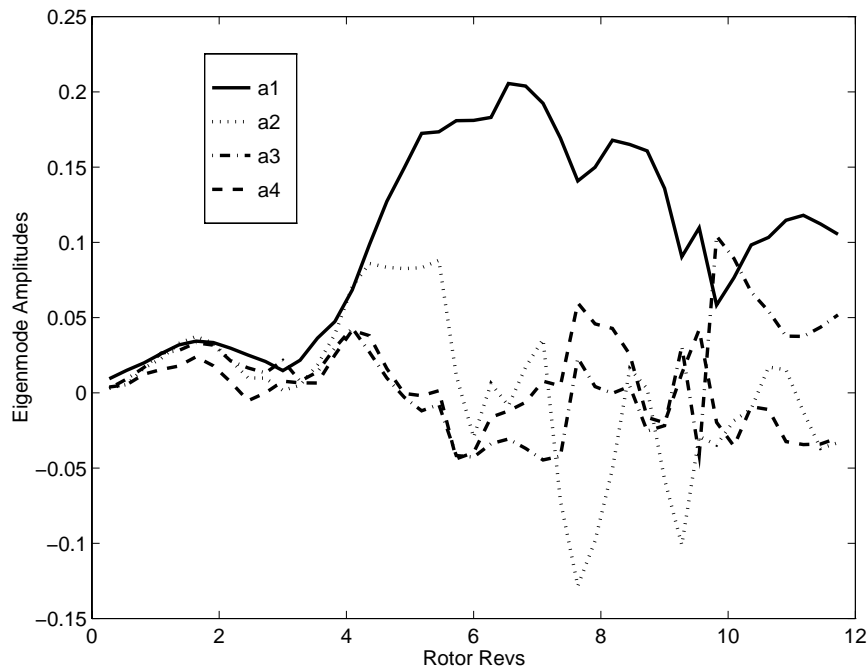


Figure 7: Contribution of the first four eigenmodes to the snapshots collected during stall inception.

possible, and this holds true for the example presented since

$$\begin{bmatrix} \lambda_1 = 0.7179 \\ \lambda_2 = 0.1212 \\ \lambda_3 = 0.0679 \\ \lambda_4 = 0.0313 \\ \lambda_5 = 0.0189 \\ \lambda_6 = 0.0131 \\ \lambda_7 = 0.0095 \\ \lambda_8 = 0.0052 \\ \vdots \end{bmatrix}$$

showing that nearly 96% of the energy is captured in the first five modes.

These empirically determined eigenmodes can now be used to decompose snapshots of the dynamically changing flow field to quantify growth rates of these modes as the stall cell develops. Projecting snapshots of the flow field onto the basis functions gives the values of the mode amplitude coefficients of (4); results are shown in Fig. 7.

One can reverse the decomposition procedure and reconstruct the flow field from mode amplitudes and the empirical eigenfunctions, such as shown in Fig. 8. This is more than simple data compression, since we see that the first mode may provide a more efficient better way of representing the flow asymmetry than the first term in a trigonometric, wavelet, or other theoretical basis function series since it captures 72% of the disturbance energy. Analogous to the Galerkin procedure used by [1], we can use these empirical eigenfunctions as a basis for discretizing the original equations of fluid motion giving nonlinear mode-amplitude equations which should predict the bifurcations and dynamics in the neighborhood of where the snapshots were collected. In fact, the eigenmodes of Fig. 6 can be used without modification for discretizing the model of Moore and Greitzer [1].

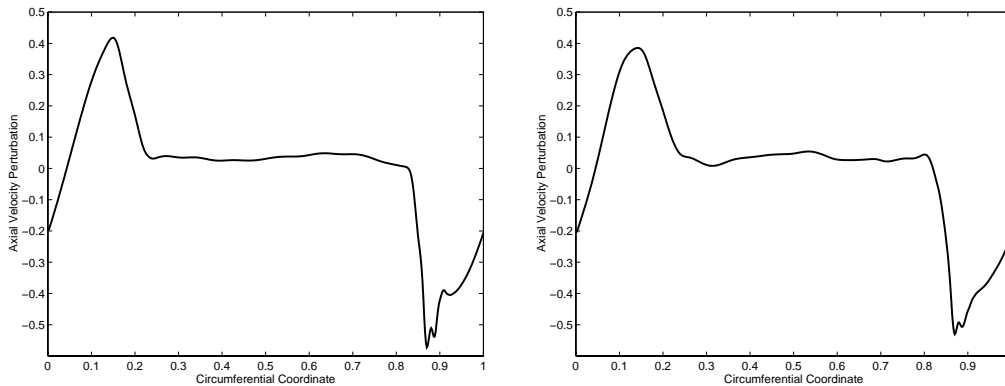


Figure 8: Axial flow deviation from mean (left) and flow deviation reconstructed from the first eight modes (right) corresponding to the flow field at rotor revs=6 of Fig. 2.

The flow field disturbances can be faithfully reconstructed for more developed rotating stall cells and the small amplitude disturbances at stall inception. Figure 9 is a stall inception disturbance (c.f. Fig. 5, the true disturbance) reconstructed from the same eight eigenmodes of Fig. 6, showing the initial flow disturbance is localized to several blades. It is interesting to see that the blade passage-width oscillations grow in amplitude to the side of the main flow deviation corresponding to the higher angle of attack (the circumferential coordinate range spanning 0.8 to 1.0 and then continuing from 0.0 to 0.2) and are suppressed on the other side (0.4 to 0.8), in accordance to the stall cell propagation mechanisms discussed.

5 Acknowledgments

This research was supported by AFOSR grant F49620-93-1-0186. This work was supported in part by a grant of HPC time from the DoD HPC Shared Resource Center, Army HPC Computing Center CM5, and the University of Maryland UMIACS CM5.

References

- [1] F. K. Moore and E. M. Greitzer, “A theory for post-stall transients in axial compression systems: Part I – Development of equations,” *ASME Journal of Engineering for Gas Turbines and Power*, Vol. 108, pp. 68-76, 1986.
- [2] M. W. Davis, Jr. and W. F. O’Brien, “Stage-by-stage poststall compression system modeling technique,” *AIAA Journal of Propulsion*, Vol 7, pp. 997-1005, 1991.
- [3] D. Goldstein, R. Handler, and L. Sirovich, “Modeling a no-slip flow boundary with an external force field,” *Journal of Computational Physics*, Vol. 105, pp. 354-366, 1993.
- [4] C. S. Peskin, “Numerical analysis of blood flow in the heart,” *Journal of Computational Physics*, Vol. 25, pp. 220-252, 1977.
- [5] T. Iura and W. D. Rannie, “Experimental investigations of propagating stall in axial-flow compressors,” *Transactions of ASME*, Vol. 76, pp. 463-471, 1954.
- [6] J. P. Longley, “A review of nonsteady flow models for compressor stability,” *ASME Journal of Turbomachinery*, Vol. 116, pp. 202-215, 1994.

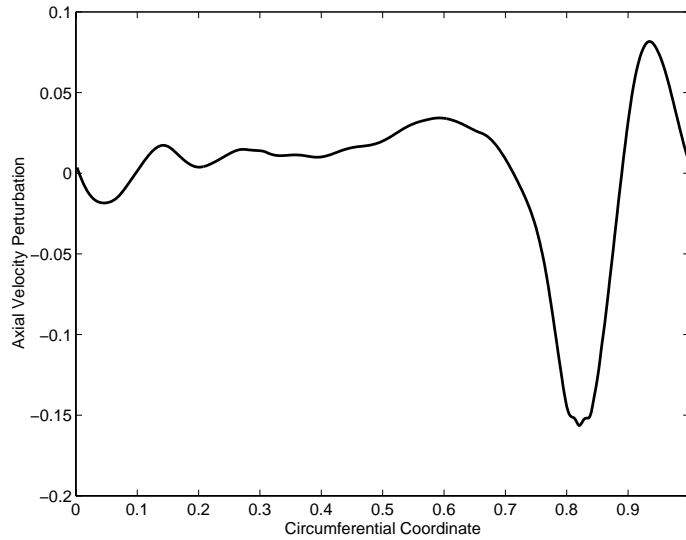


Figure 9: Stall inception perturbation reconstructed from the first eight empirical eigenmodes.

- [7] O. O. Badmus, S. Chowdhury, K. M. Eveker, C. N. Nett, and C. J. Rivera, "A simplified approach for control of rotating stall: Experimental results," *AIAA paper 93-2234*, 1993.
- [8] R. Peyret and T. D. Taylor, *Computational Methods for Fluid Flow*. Springer-Verlag, New York, 1983.
- [9] G. E. Karniadakis, M. Israeli, and S. A. Orszag, "High-order splitting methods for the incompressible Navier-Stokes equations," *Journal of Computational Physics*, Vol. 97, pp. 414-443, 1991.
- [10] R. A. Adomaitis and E. H. Abed, "Local nonlinear control of stall inception in axial flow compressors," *AIAA paper 93-2230*, 1993.
- [11] L. E. Sirovich, "Turbulence and the dynamics of coherent structures, Part I: Coherent Structures," *Q. Appl. Math.* Vol. XLV, pp. 561-571, 1987.